

Amplification of Shear Layer Instability by Vorticity Generation at an Injecting Wall

Jérôme Vétel,* Frédéric Plourde,[†] and Son Doan Kim[‡]

Ecole Nationale Supérieure de Mécanique et d'Aérotechnique, 86960 Futuroscope Cedex, France

The influence of an emerging obstacle on a constant sidewall injection flow is investigated. The confined chamber where the flow develops acts as a resonator; a nozzle placed in the flow exit represents an impingement area for vortices to favor the occurrence of a feedback phenomenon. When the obstacle height is one-quarter of the channel height, the shear layer generated in its wake reattaches some distance downstream, and relatively intense vorticity is generated at the sidewall. The resulting structures have the characteristics of wall vortices, and the flowfield behaves like a well-known injecting flow without obstacle. The flow patterns generate sound through a feedback loop that drives the shear layer oscillations at separation. A study of the interaction between the shear layer and the injected flow is conducted by increasing the height of the obstacle. Under a low-frequency forcing by pressure waves, a pairing process occurs before reattachment, and the frequency halving allows sustainment of the frequency stages of the feedback phenomenon. Finally, for high obstacle height, the shear layer no longer reattaches, the vorticity generation disappears, and a reduction of the resonance is observed.

Nomenclature

a	= sound velocity, m/s
f_n	= n th longitudinal acoustic mode, $na/2\ell$, Hz
H_c	= channel height, m
H_{obs}	= obstacle height, m
It	= turbulence intensity, $\sqrt{(u'^2 + v'^2)}/aM$
L	= distance between the obstacle and the nozzle locations, m
ℓ	= channel length, m
M	= characteristic Mach number based on the mass flow rate, $q_m/apwH_c$
M_c	= convection Mach number of coherent structures
p	= mean pressure at the front head, Pa
q_m	= total mass flow rate, kg/s
$R_{x'y'}$	= correlation coefficient of arbitrary functions of time x' and y' , $\overline{x'(t) \cdot y'(t + \tau)}/\sqrt{[x'(t)^2][y'(t)^2]}$
Str	= Strouhal number, fL/aM_c
$S_{x'}$	= normalized power spectral density $s_{x'}/\overline{x'^2}$, Hz^{-1}
$s_{x'}$	= power spectral density
T	= period, s
U	= normalized mean velocity, \bar{u}/U_{\max}
U_{\max}	= maximum longitudinal velocity in each section
u, v	= velocity component in X and Y directions m/s
w	= channel width, m
X, Y	= nondimensional axis normalized, respectively, by L and H_c
ε	= geometric parameter, H_{obs}/H_c
ρ	= density, kg/m^3
τ	= time delay, s

Superscripts

$'$	= fluctuating component
$-$	= time averaged
$\langle \rangle$	= phase averaged

I. Introduction

Flows induced by sidewall injection are newly viewed because the wall vortex-shedding phenomenon has been found to be an important instability mechanism. The studies of flows generated through porous material were, in particular, prompted by a need to understand the internal aerodynamic developing inside solid-propellant motors. In a two-dimensional porous wall duct, Traineau et al.¹ specified three regions of flow development that supported the previous observations of Beddini²: The laminar region governed by the injection is followed by a transition region, where velocity fluctuations appear near the centerline and move toward the injecting wall. Then a region dominated by the compressibility effects develops. In these experiments, even for the turbulence transition region, mean velocity profiles show fair agreement with those derived by Taylor³ and Culick⁴ for a steady, incompressible and inviscid flow injected normal to the surface. However, Yeh et al.⁵ showed that the axial flow transition, as well as the velocity profile, depends on the porous material characteristics and, especially, the pseudo-injected turbulence generated by the pores of the porous wall. The experimental setups that allow for study of the interaction between a main flow and a wall injecting flow were particularly useful in characterization of the turbulence. Whereas Yagodkin⁶ observed the stabilizing effect of injection, Varapaev and Yagodkin⁷ developed a linear hydrodynamic stability theory for injection-induced flows. They showed that, in addition to the classical axial Reynolds number, flow stability also depends on the injection Reynolds number, based on the injection velocity. Moreover, they were able to indicate a relation between the critical axial Reynolds number and the injection Reynolds number. For axisymmetric channels, Eckert and Rodi⁸ and Pennell et al.⁹ used the injection Reynolds number effect to turn a turbulent flow to laminar. The transition from laminar to turbulent was observed some distance downstream for a critical axial Reynolds number one order of magnitude larger than for a channel with impermeable walls. However, despite the introduction of the hydrodynamic instability concept in such flows, the results obtained by Varapaev and Yagodkin⁷ were attributed only to the turbulence transition effects. Flow development and transition to turbulence were thoroughly analyzed by Dunlap et al.¹⁰ in a cold-flow setup of a solid rocket motor. They were the first to mention a possible unstable mechanism occurring at the injecting wall because of

Received 23 November 2002; revision received 8 July 2003; accepted for publication 8 July 2003. Copyright © 2003 by the American Institute of Aeronautics and Astronautics, Inc. All rights reserved. Copies of this paper may be made for personal or internal use, on condition that the copier pay the \$10.00 per-copy fee to the Copyright Clearance Center, Inc., 222 Rosewood Drive, Danvers, MA 01923; include the code 0001-1452/04 \$10.00 in correspondence with the CCC.

*Postdoctoral Researcher, Laboratoire d'Etudes Thermiques, Téléport 2, 1 Avenue Clément Ader, BP 109.

[†]Senior Research Scientist, Centre National de la Recherche Scientifique, Laboratoire d'Etudes Thermiques, Téléport 2, 1 Avenue Clément Ader, BP 109. Member AIAA.

[‡]Professor, University of Poitiers and Laboratoire d'Etudes Thermiques, Téléport 2, 1 Avenue Clément Ader, BP 109.

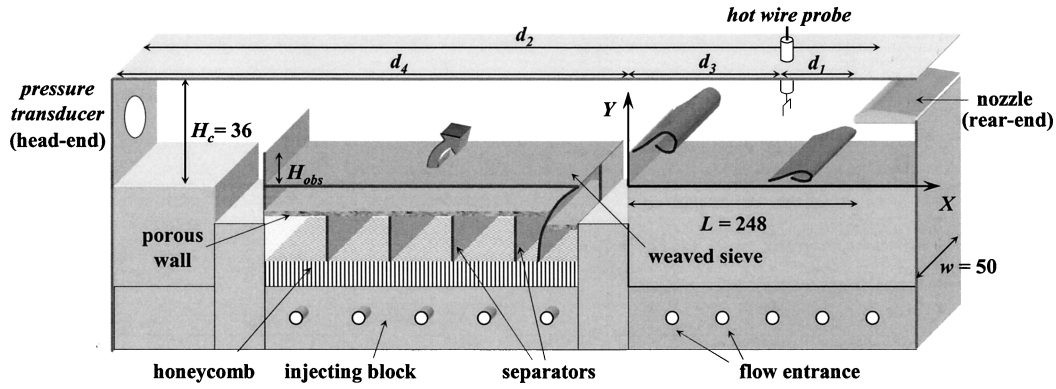


Fig. 1 Schematic of the experimental setup.

their unsteady measurements. However no implications were drawn from these results. In a numerical simulation of solid rocket motors, Lupoglazoff and Vuillot¹¹ depicted the wall vortex-shedding phenomenon as an important source of acoustic energy. Their work was the first to mention that the wall vortices could drive motor instabilities, providing a reason for the unexplained unstable behavior observed during the firings. The stability theory was then reintroduced in injection-induced flows for planar¹² and axisymmetric¹³ channels and compared with the experimental results of Avalon et al.¹⁴ The vortex shedding that occurs at the injection surface was considered in these works as arising from a hydrodynamic stability mechanism. Other works attribute the generation of vorticity patterns near the wall to an interaction between the local axial pressure gradient at the surface and the injected fluid. Majdalani and Van Moorhem¹⁵ discussed this process for small-pressure-gradient amplitude. The impact of large pressure disturbances was likewise treated in a non-linear context by Kirkkopru et al.,¹⁶ Zhao et al.,¹⁷ and Staab et al.,¹⁸ using asymptotic analyses and numerical results.

A few experimental findings are known concerning the influence of an obstacle placed in an injection-induced flow. With use of a time-dependent two-equation model, Shu et al.¹⁹ characterized the recirculating flow behind the obstacle and compared the vortex-shedding frequencies at separation with experiments. Vetel et al.^{20,21} studied the flowfield inside a 1/40-scale model of the solid-propellant booster of Ariane 5. The cold-gas simulation was able simultaneously to reproduce a vortex shedding in the wake of an obstacle and a wall vortex shedding in the vicinity of the sidewall injection. They showed that frequency stages occur in the shear layer generated at the top of the obstacle due to a feedback phenomenon. The wall vortex shedding was characterized by broadband spectra, whose central frequency increases linearly with the Mach number. Moreover, they demonstrated that this wall instability was responsible for pressure wave generation by impingement of wall vortices on the nozzle in the rear end of the chamber. On the other hand, the receptivity of wall velocity fluctuations to pressure waves was not observed, which means that no frequency stages were observed on velocity spectra by increasing the Mach number, that is, the coupling phenomenon between the wall instability and the pressure oscillations did not occur.

The aim of this study is to spotlight another unsteady process that could occur in a flowfield generated by constant sidewall injection in a chamber with an emerging obstacle. The experimental setup is the one already used by Vetel et al.²⁰ To favor wall vortex development and the injection effects, the height of the channel was increased. Flow development is described in terms of mean and fluctuating characteristics. A study of the influence of the obstacle height is then performed.

II. Experimental Apparatus and Measuring Techniques

Complete details of the experimental system was described by Vetel et al.²⁰; relevant aspects of the geometry and the measuring techniques are briefly summarized here, and data processing is

given. The scale model ($\ell = 623$ mm) does not completely reproduce the actual full-scale motor but is roughly similar through the presence of segmented blocks and a submerged nozzle. As shown in Fig. 1, two injecting blocks are located in the chamber separated by an embedded obstacle of 9 mm height. The flow is generated by injecting air at ambient temperature from a feeding unit, whose mass flow rate is fixed at $q_m = 0.105$ kg/s. Injection into the channel is carried out through a porous wall characterized by a sintered-bronze sphere Poral plate with $2\text{-}\mu\text{m}$ characteristic diameter and a flexible metallic weaved sieve set at 10 mm above the Poral plate. The uniformity of the mass flow rate distribution along the porous wall is controlled by a feeding system. For each injecting block, airflow is fed into a general manifold divided into 10 flexible polyamide tubes. In their turn, these tubes feed an isolated cell, and the mass flow rate in each injection cell is controlled by sonic air inlets. The Poral plate isolates the flow in the chamber, whereas the metallic weaved sieve significantly reduces the injected turbulence in the chamber. A nozzle is located at the rear end of the chamber to ensure the acoustic isolation of the channel from the outer environment. The height of the nozzle throat can be varied, thereby controlling the mean Mach number M in the chamber.

The mean and fluctuating pressure signals are measured at the head end with a flush mounted 7261 Kistler piezoelectric quartz transducer with a static pressure accuracy of 10 Pa. The dynamic response provides a fluctuating pressure sensitivity of about 0.02 Pa. The velocity signals are recorded from a Dantec $5\text{-}\mu\text{m}$ single miniature probe for spectral analyses and from a $5\text{-}\mu\text{m}$ X miniature probe for mean flow characterization. The uncertainty of the mean velocity was estimated to be equal to $\pm 1\%$ and that of the fluctuating component to $\pm 2.5\%$. The injected air temperature is obtained by a K thermocouple, and the mass flow rate ($\pm 2\%$) is controlled by a measure of the pressure drop through a diaphragm placed downstream from the feeding unit. The calibration procedure and the accuracy of the measurements are given in detail in Ref. 21.

All of the signals are recorded by a 12-bit AT MIO-16E10 A/D board with a SC 2040 submitting sampling data. The mean and fluctuating quantities are sampled differently to improve the accuracy. The sampling frequency used is 10 kHz, whereas the maximum frequencies of the pressure and velocity fluctuations were found to be below 1000 Hz. All data analyses are made by postprocessing. The time-averaged mean quantities are obtained over 4-s time length data records with an accuracy of $\pm 1\%$. Spectral analyses are performed by a fast Fourier transform (FFT) algorithm. The power spectral density is constructed by averaging 50 spectra, each calculated with 4096 data points, and provides a frequency resolution of 2.44 Hz. The total data record is also used to calculate the time-averaged rms values. To suppress the anomalies introduced by the finite Fourier transforms in the estimated spectra, a full cosine tapering window, that is, a Hanning window, is introduced for each FFT calculation. This time window tapers the data to allow a more gradual entrance to and exit from the time history data. To retrieve some of the diminished statistical accuracy of the analyzed results, an overlap averaging procedure is used. Furthermore, the autospectral density functions are normalized by the rms value of the analyzed

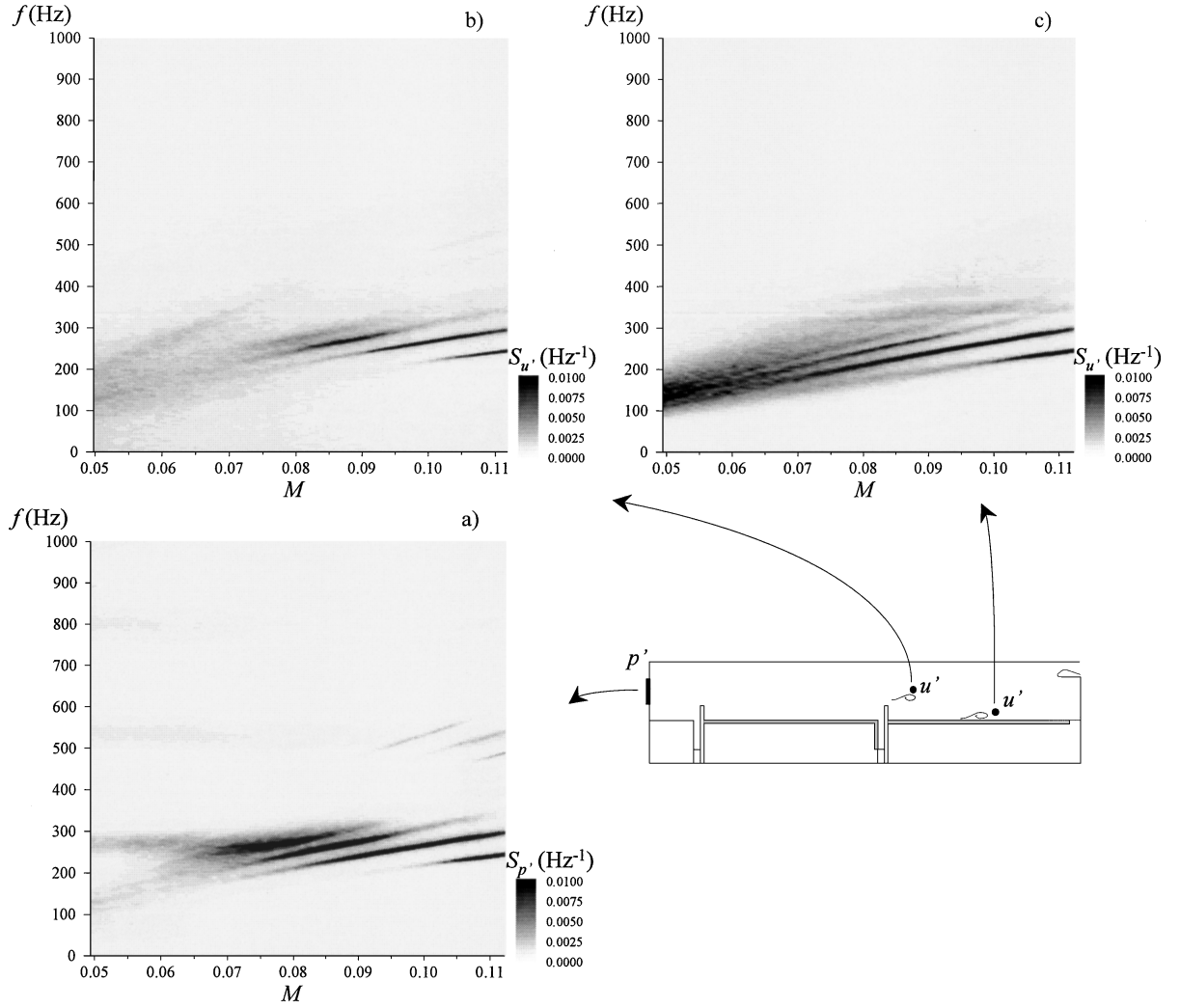


Fig. 2 Evolution of a) pressure spectra at head end and velocity spectra b) in the wake of the obstacle and c) in the vicinity of the injecting wall.

data. Therefore, the average spectra provide the mean properties of the vortex-shedding process, as well as the resonance phenomenon.

The auto- and cross-correlation functions are estimated by computing the finite inverse Fourier transform of auto- and cross-spectral density functions. The bias error due to the circular effect introduced by this calculation procedure is eliminated by extending the time record with an additional zero value record segment of the same length.²² The random error is estimated to be $\pm 0.1\%$. When the data are sinusoidal or narrowband random in character, the time delays corresponding to the maximum of the correlation coefficients are difficult to extract. The envelop functions are then computed via the Hilbert transform of the correlation functions.

Phase-averaged quantities are obtained from the same record length as spectral estimates. The procedure consists of averaging the instantaneous velocity signals for a number of cycles typically of the order of 2500. The phase averaging is obtained over one period, which is subdivided into 80 time intervals. Each interval is then the result of approximately 2500 ensemble averages. Although considerable effort went into ensuring the accuracy of the data, the purpose of the phase-averaged results is to present qualitative insights into the vortex development and quantitative information through comparisons between the different measurement points.

III. Results and Discussion

A. Fluctuating Flowfield Investigation

Assume first that, despite the modification of the channel height, the two hydrodynamic instabilities are still present with regard to

previous results.^{20,21} Figure 2 presents simultaneously the evolution of velocity and pressure spectra as the Mach number increases. The pressure fluctuations (Fig. 2a), recorded at the head end of the chamber, are mainly characterized by a concentration of energy around the first acoustic mode of the chamber ($f_1 = 280$ Hz). For $M < 0.07$, the normalized spectra are broadband, but for higher Mach number levels, a strong acoustic resonance appears. The spectral peak at $f = f_1$ becomes narrow band, and several stages occur for which the frequency linearly increases with M . The stages observed are not actually separated by frequency jumps because, for almost the whole Mach number range, pressure signals oscillate at two defined frequencies; nonetheless, spectra show the presence of one single peak for $0.095 < M < 0.105$. Velocity spectra (Fig. 2b), recorded close to the obstacle location ($X = 0.15$, $Y = 0.47$), indicate that the spectral organization of velocity fluctuations is similar to that of pressure fluctuations at the head end. For $M > 0.07$, the four frequency stages are present, whereas for $M < 0.07$, the flowfield is much less organized. The comparison of the shear layer oscillations with the pressure fluctuations, therefore, shows that a feedback phenomenon occurs because of the impingement of vortices on the nozzle in the rear end of the chamber, as previously observed.²⁰ Note that close to the injecting wall ($X = 0.64$, $Y = 0.05$, Fig. 2c) and for $M < 0.07$ spectra are broadband and the involved frequencies increase with M . Therefore, either a natural wall instability develops in the vicinity of the injecting wall, or vorticity generation arises from the interaction between the pressure gradient and the injected flow. Because this region is disturbed by the flowfield fluctuations downstream from the obstacle and because the separation

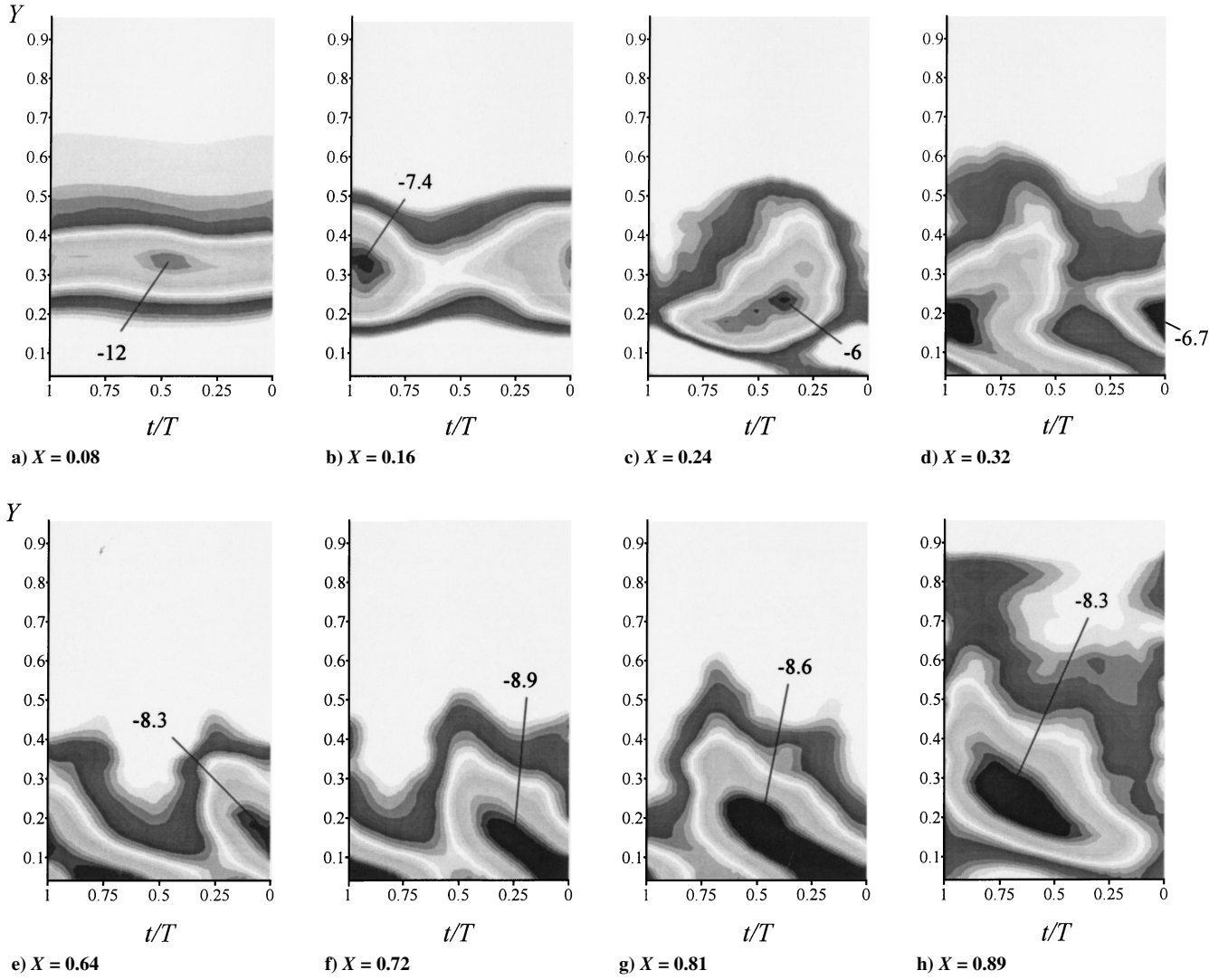


Fig. 3 Phase-averaged vorticity data for different axial locations.

point can move slightly from one position to another, wall vortex shedding is not a steady harmonic process. It is rather a series of coherent strings of events, whose frequencies wander about the nominal vortex-shedding frequency. On the contrary, for $M > 0.07$, sharp, narrowband peaks appear. Velocity spectra also present frequency stages, which seems to indicate the presence of a coupling phenomenon between wall vortex shedding and pressure waves. According to Blevins,²³ who studied the effect of sound on vortex shedding from cylinders, the applied pressure waves near the natural frequency synchronize the vortex-shedding process to the forcing acoustic frequency, and therefore, frequency wander is eliminated.

The presence of similar frequency stages in the shear layer and close to the wall injection shows that the two vortex developments are linked. Under these conditions, some assumptions may be put forward. First, pressure fluctuations are driven by the shear layer instability, which drives the other instability as well. In this case, the pressure oscillations have no effect on the wall instability. This may be possible because the pseudoinjected turbulence at the injecting wall can weaken the effect of acoustic waves. Second, the two velocity fluctuations recorded in the wake of the obstacle and in the vicinity of the porous wall correspond to the same phenomenon, that is, the behavior of wall velocity fluctuations is a consequence of the induced field produced by the shear layer vortices. Under strong acoustic oscillations, the growth rate of the shear layer is increased, resulting in large-scale structures. Third, it may be possible to have a coalescence phenomenon between vortices from two different instabilities. The upstream-propagating pressure wave triggers the shedding of a wall vortex, then a shear layer vortex. The

latter convects more quickly than the former because the convection occurs in a higher speed region, and the two vortices merge.

To gather more information about the kind of unstable mechanism occurring in the flow, phase-averaged vorticity Ω_z is shown in Fig. 3 with data obtained at $M = 0.1$, where the velocity fluctuation spectrum contains only one dominant frequency. The eductions were done at four locations downstream from the obstacle location and at four locations in the rear end of the chamber, and the contours of Ω_z are shown as a function of time and distance. Phase-averaged longitudinal and transverse velocities $\langle u \rangle$ and $\langle v \rangle$ were first obtained with the X-wire probe as a function of time t and location Y . Pressure signal from the head end served as the reference signal. Ω_z was then obtained via Taylor's hypothesis, using the equation

$$\Omega_z = -\frac{\partial \langle u \rangle}{\partial y} - \frac{1}{aM_c} \frac{\partial \langle v \rangle}{\partial t} \quad (1)$$

where M_c is the mean convection Mach number of vortices, calculated in Sec. III.C. The time t and vorticity Ω_z have been nondimensionalized by the period T and the frequency of the phenomenon, respectively. As seen in Fig. 3, in the vicinity of the obstacle ($X = 0.08$), results spotlight the unstable layer formation after separation. By a rollup mechanism, large-scale structures develop, as can be seen at location $X = 0.16$. At $X = 0.24$, the shape of the structure is not as regular as the contours observed at $X = 0.16$, and the center of the vortex moves toward the injecting wall as X increases. This trend is confirmed at the next location ($X = 0.32$), where near-wall large-scale coherent structures are observed. They are characterized

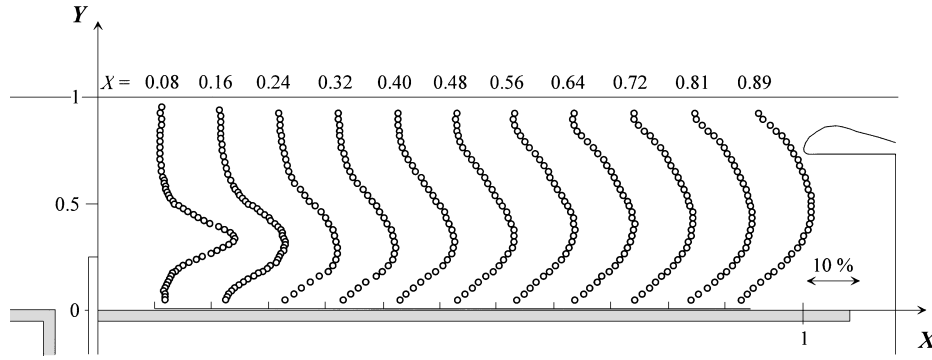


Fig. 4 Turbulence intensity distribution.

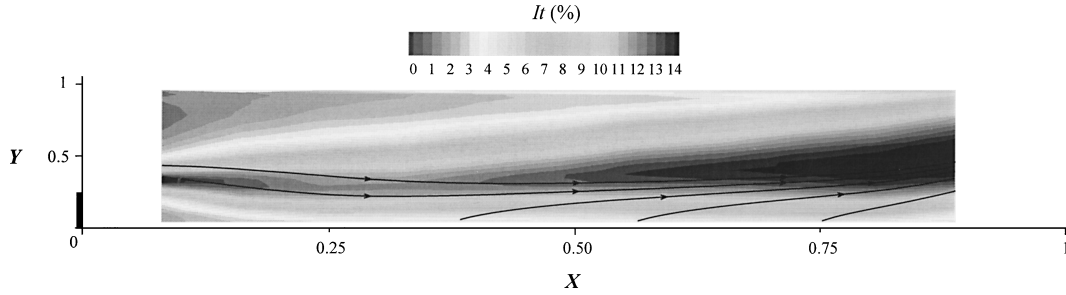


Fig. 5 Map of turbulence intensity contours and streamlines.

by elongated vorticity regions inclined at an opposite angle compared with the mean flow direction. The convection of these vortices is then clearly observed in a region near the porous wall up until the rear end of the chamber. At the same time, the vorticity magnitude, which decreases in Figs 3a–3c, has an opposite trend from $X = 0.24$ to $X = 0.72$. Finally, at the last location studied ($X = 0.89$), vortices separate from the wall before reaching the nozzle location. These results, therefore, show that the shear layer vortex development is amplified thanks to vorticity generation in the vicinity of the injecting wall, resulting in the presence of only one instability in the flow.

Such needle-shaped vortical structures developing along the injecting wall are typical of wall instability as observed from experimental,²⁴ as well as numerical, simulations^{11,25} conducted on wall injected flows in channels without geometric disparities. However, the aspect ratio of the chamber is not favorable enough for such behavior to occur.²⁰ Consequently, according to linear stability theory, a wall instability should not be observed. The vorticity generation may be a consequence of an interaction between the axial pressure gradient and the injecting flow, corroborating theoretical and numerical results from recent works,^{16,18} rather than arising from classical hydrodynamic instabilities that are precursors of turbulence. In particular, Zhao et al.¹⁷ showed a vector field plot with an elongated vortex structure against the injection surface. Thus, in the present study, the current experiments appear to show that the pressure transient induced by the obstacle shedding is the primary cause of vorticity generated at the injection surface. However, the fact remains that the vortices behave like wall vortices in the rear end of the chamber. To examine this kind of flowfield closely, the mean flow characteristics are studied in the next section.

B. Mean Flow Characterization

The profiles of the turbulence intensity It are presented in Fig. 4 for several positions downstream from the obstacle location. At $X = 0.08$, the profile shape is characterized by a peak that results from the shear layer formation. The transverse location of the maximum of It is at $Y \approx 0.3$, higher than the top of the obstacle. By the increase of the distance X , the spatial expansion of the shear layer is observed, especially for the small Y locations. The peak grows

larger, and the maximum moves toward the injecting wall, to reach at $X = 0.24$, the same Y location as the top of the obstacle. Then, for $0.24 < X < 0.89$, the trend is inverted. The location of the maximum of It moves away from the injecting wall, and at $X = 0.89$, this maximum location reaches half the height of the channel. For this last axial location, the profile is almost symmetric with regard to the midheight of the channel; the presence of velocity fluctuations throughout the height of the channel shows the strong instability as well as the large-scale structure development.

Figure 5 traces the changes of the turbulence intensity in the two spatial directions in the form of a contour map. When the transverse location of the maximum of It in each section moves toward the injecting wall ($0 < X < 0.25$), the level of It decreases. On the contrary, downstream from $X \approx 0.25$, the distance between this maximum and the injecting wall increases, and at the same time, the turbulence intensity magnitude increases to reach over 14% in the rear end of the chamber. As shown in Fig. 3, the generation of vorticity at wall coincides with an increase in the velocity fluctuation levels. Some streamlines are also drawn in Fig. 5, computed from the mean velocity field. Despite the presence of the obstacle, the streamlines bypass the top of the obstacle and move toward the injecting wall. Then, in the second half of the channel, the streamlines converge in the direction of the nozzle location. Therefore, in view of the flapping nature of the flowfield, the shear layer has a streamline curvature and reattaches on the injecting wall some distance downstream from separation. In its overall structure, the shear layer, thus, resembles the separated flow past a backward-facing step or a rib.²⁶ Yamada et al.²⁷ studied in detail and correlated the turbulence intensity distributions with the erosive burning phenomenon in a flowfield generated by porous wall injection. They showed that downstream from a laminar region, a transient region is characterized by the appearance of irregular velocity fluctuations. The distance between the maximum value of the turbulence intensity and the wall decreased as the axial location increased. After which, a turbulent region development was observed. The same results were obtained by Dunlap et al.,¹⁰ but in addition to these observations, oscillation behavior was suggestive of vortical disturbances. Downstream, the turbulence profiles were seen to gradually bloom out toward the centerline with increasing axial position. Moreover, axial velocity profiles are in agreement

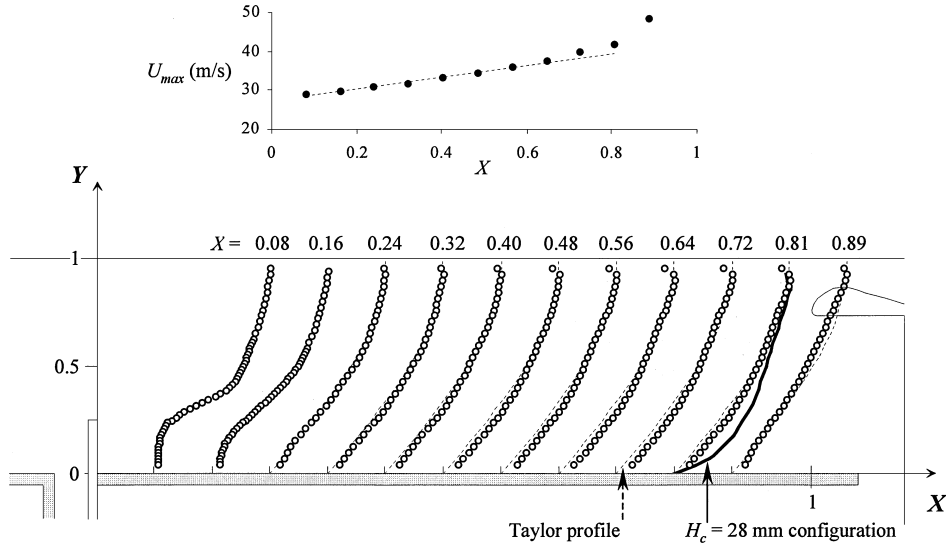


Fig. 6 Nondimensional axial velocity distribution at various locations.

with analytical predictions of an inviscid flow satisfying the no-slip boundary condition.

The mean axial velocity field is shown in Fig. 6. For the first profile presented ($X = 0.08$), the shear layer development is pointed out by a large transverse velocity gradient in the wake of the obstacle. Flow destabilization, characterized by an inflexion point on the velocity profile, is also observed at $X = 0.16$. At $X = 0.24$, this perturbation is much less observable, to such a degree that at the next location ($X = 0.32$) the inflexion point has disappeared. For $X > 0.32$, the shape of the profile does not change significantly. The velocity increases regularly from the injecting wall, to the upper wall, where the boundary layer develops as X increases. The theoretical profiles, calculated by Taylor³ for an injecting channel flow without geometric disparities, are also compared with the experimental results, and a quite satisfactory agreement is observed. The maximum of the axial velocity in each section is also shown in Fig. 6 vs the X location. Almost throughout the length of the chamber, the evolution is linear. For the last positions ($X > 0.72$), the flow is accelerated due to the presence of the nozzle exit at the rear end of the chamber. With this characteristic evolution of U and U_{max} , the flow properties agree with the Taylor flow. Despite the presence of an obstacle, the flowfield behaves here like the one studied by Dunlap et al.¹⁰ The obstacle represents an excitation source that forces the turbulence development, and its perturbation on the flow reproduces all of the characteristics of the transient region observed in injection-driven flows. Downstream, the flowfield can be compared with a wall duct flow unperturbed by the obstacle, where wall instability would be observed upstream from the natural triggering location. To compare the results between the two different channel heights, the nondimensional velocity profile obtained for $H_c = 28$ mm in a previous study²⁰ is likewise shown in Fig. 6 for $X = 0.81$. This velocity profile does not match with the theory, even far downstream from the obstacle location. In fact, in this configuration, the shear layer does not reattach. In addition to the wall instability, vortices are shed at flow separation at the top of the obstacle and develop independently of wall vortices. Furthermore, the deviation of the velocity profile from the theory may arise from more turbulent behavior due to a lower injection Reynolds number.

C. Identification of the Instability Process

To describe the coupling phenomenon thoroughly, Vétel et al.²⁸ used the cross-correlation coefficients between velocity and pressure oscillations. They showed that, for a velocity signal recorded in the fluctuating flowfield and a pressure signal recorded at the head end of the chamber, each of the two branches of the feedback loop is described by a time delay for which a maximum of $R_{u'p'}$ is obtained. The presence of a positive time delay τ^+ means that pressure waves

are generated by vortex–nozzle interaction, whereas a negative time delay τ^- is related to the shear layer acoustic forcing at separation (Fig. 1):

$$\tau^+ = d_1/aM_c^+ + d_2/a \quad (2)$$

$$\tau^- = -d_3/aM_c^- + d_4/a \quad (3)$$

where M_c^- is the mean convection Mach number between the obstacle location and the velocity probe and M_c^+ the mean convection Mach number between the velocity probe and the nozzle location. Two examples are shown in Fig. 7 with the velocity probe located at ($X = 0.31$; $Y = 0.05$). At $M = 0.09$, the cross-correlation coefficient is characterized by a trigonometric shape, where a negative τ^- as well as a positive τ^+ time delay is clearly observed. At $M = 0.1$, the oscillatory shape of the $R_{u'p'}$ coefficient is particularly pronounced because, for this Mach number and as already shown, the instability mechanism is described by only one frequency. The evolution map of $R_{u'p'}$ with M points out the presence of the τ^+ and τ^- time delays by the τ_0^+ and τ_0^- time delays. Time delay τ_0^+ is observed whatever the Mach number, which means that vortices generate pressure waves after impingement on the nozzle. On the contrary, τ_0^- appears only for $M > 0.075$ because pressure waves influence the vortex shedding at separation for this Mach number range. However, several additional time delays for which the $R_{u'p'}$ levels are significant are also observed. Peaks of correlation regularly spaced in time are present for positive time delays, called τ_n^+ , as well as negative time delays, called τ_n^- . Some assumptions can be made about these time delays. Time delay τ_0^+ is the time required for a vortex to convect from the hot-wire probe to the nozzle location, plus the time delay for the pressure wave generated by vortex impingement to travel upstream as far as the front head of the chamber. By the addition of one period of the feedback loop, τ_1^+ may express that, before reaching the head end, the pressure wave interacts with the top of the obstacle, triggering another vortex formation, which convects and impinges on the nozzle generating another pressure wave. This second pressure wave would be the one captured at the head end by the pressure transducer. By the addition of several cycles to the phenomenon, the time delay τ_n^+ can be written

$$\tau_n^+ = d_1/aM_c^+ + n(d_1 + d_3)(1/a + 1/aM_c) + d_2/a \quad (4)$$

or

$$\tau_n^+ = \tau_0^+ + n\Delta\tau \quad (5)$$

with

$$\Delta\tau = L/a(1 + 1/M_c) = \tau_0^+ - \tau_0^- \quad (6)$$

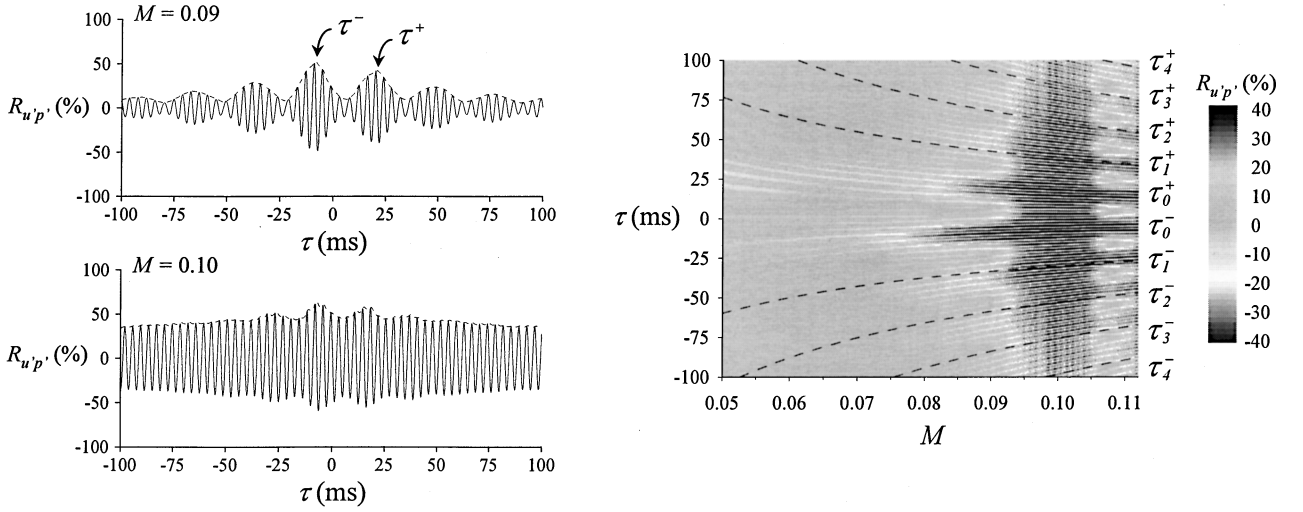


Fig. 7 Cross-correlation coefficients between pressure fluctuations and wall velocity fluctuations.

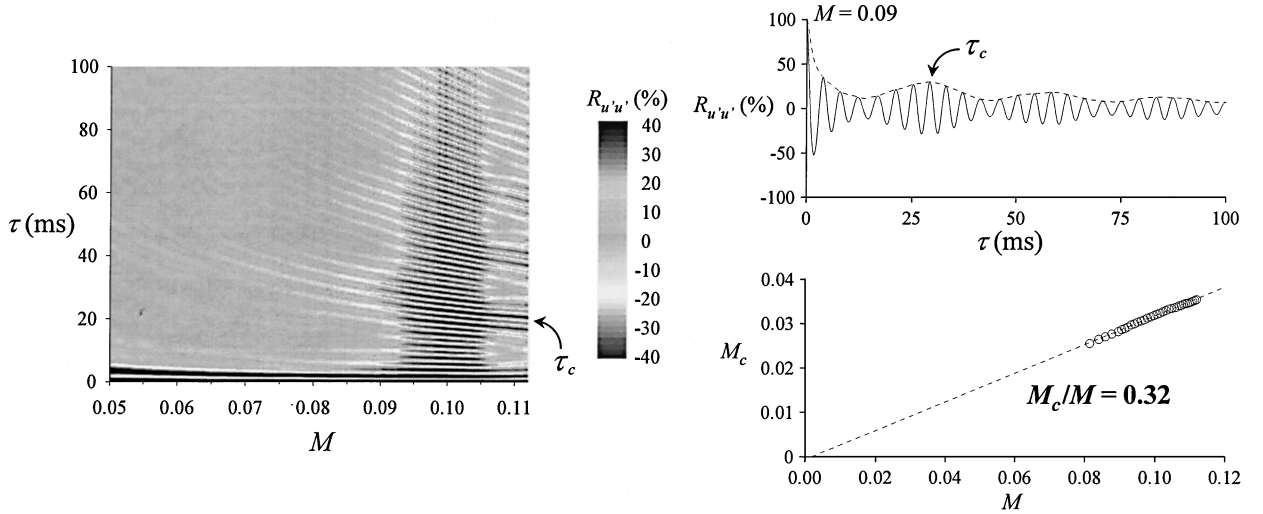


Fig. 8 Velocity autocorrelation coefficients and estimation of the mean convection Mach number.

where M_c is the mean convection Mach number defined by

$$(d_1 + d_3)/M_c = d_1/M_c^+ + d_3/M_c^- \quad (7)$$

By analogy, τ_n^- can be written

$$\tau_n^- = \tau_0^- - n\Delta\tau = \tau_0^+ - (n+1)\Delta\tau \quad (8)$$

When Eq. (6) was used, the time delays τ_n^+ and τ_n^- have been calculated by Eqs. (5) and (8), respectively, and plotted with the evolution of $R_{u'p'}$ in Fig. 7. A satisfactory agreement is observed between measured and calculated time delays. The presence of these correlations provides more information about the fluctuating flowfield. First, the coherent part of the velocity signal is conserved between separation and impingement, which supports the finding that the coherent structure appearing after reattachment is the same as the shear layer vortex. The resulting vortex is, thus, fed by vorticity generation because the injected flow, instead of occurring from a hydrodynamic instability in which the formation of a wall vortex merging with a shear layer vortex would be observed. Second, the presence of a high degree of signal coherence for such high time delays was not observed for the $H_c = 28$ mm case. Here, by increasing the channel height, the axial Reynolds number, based on the U_{\max} velocity and the distance H_c , is conserved, whereas the injection Reynolds number, based on the injection velocity, is increased. It is well known that the effect of the injection Reynolds number on an injected flow

is stabilizing and puts the appearance of turbulence back.^{6,7} Here, this stabilizing effect can be observed by the nature of turbulent fluctuating velocity.

Next, to gain information about the instability process, the Strouhal number Sr has been calculated. Its definition is based on the length L between separation and impingement and the convective Mach number M_c to indicate the number of periods in one cycle of the feedback loop.²⁹ The determination of the mean convection Mach number could be obtained from Eqs. (2) and (3) with Eq. (7), but to enhance the accuracy of the method, this determination was made differently, using only one equation through the definition of only one time delay. Indeed, given the high degree of velocity fluctuation coherence, M_c can be deduced from signal correlations of the same nature. The autocorrelation coefficient $R_{u'u'}$ has been estimated for the velocity probe positioned at the same location as in Fig. 7. Figure 8 provides an example of the $R_{u'u'}$ curve vs τ obtained at $M = 0.09$. Naturally, $R_{u'u'}$ is close to 1 for $\tau = 0$, but in addition, another strong correlation is obtained at the time delay τ_c . This time delay corresponds to one cycle of the feedback loop:

$$\begin{aligned} \tau_c &= d_1/aM_c^+ + (d_1 + d_3)/a + d_3/aM_c^- \\ &= L/aM_c + L/a = \Delta\tau \end{aligned} \quad (9)$$

From the evolution of $R_{u'u'}$ with M shown in Fig. 8, the Mach number M_c was calculated with Eq. (8) (Fig. 8). The linear evolution of the convective Mach number with M permits extraction of a

constant ratio $M_c/M = 0.32$, which corresponds to the convection coefficient. Then, the Strouhal number has been estimated. Figure 9 presents the distribution of the power spectral density seen in Fig. 2c as a function of M and Strouhal number S_r . For $M < 0.08$, the Strouhal numbers, based on the most excited frequencies, increase with the Mach number. However, for higher M levels, that is, when the coupling phenomenon is observed, the three frequency stages are characterized by a constant Strouhal number. Moreover, the three

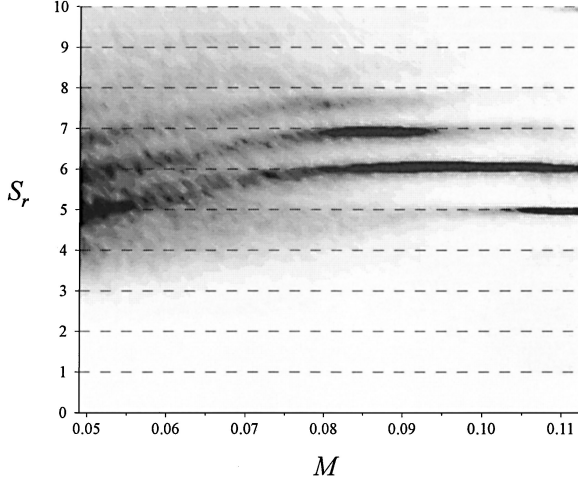


Fig. 9 Map of the power spectral density as a function of Strouhal number and Mach number.

calculated Strouhal numbers S_r correspond to three consecutive integers. An integer number of waves, that is, vortices, are, thus, present between separation and impingement for $M > 0.08$. This result consequently shows that the upstream propagating pressure waves and the coherent structures are phase locked at the top of the obstacle. Thus, despite the transformation of the shear layer vortices by vorticity generation between separation and impingement, the behavior of the feedback loop remains the same as observed in well-known impinging flows, as, for example, the impinging jet studied by Ho and Nosseir.³⁰ The feedback loop differs to some extent from a flow without obstacle. In the latter case, the pressure waves drive the wall vortex shedding at a given point located at the injecting wall,¹⁴ whereas, here, this influence is observed at the top of the obstacle. Because the wall vortices are a consequence of flow separation at the obstacle, the objective of the next section is to study different kinds of interaction taking place between the shear layer and the injecting wall.

D. Mean Flow–Injected Flow Interaction

The height of the obstacle was increased to modify the influence of the shear layer on the downstream injected flow. An initial influence can be observed in Fig. 10, which shows the spectra of pressure fluctuations recorded at the head end of the chamber. In Fig. 10, ε is a geometric parameter that represents the ratio of the obstacle height H_{obs} on the channel height H_c ; for the configuration studied in preceding sections, ε was 0.25. For $\varepsilon = 0.3$, no great differences are observed compared with the case $\varepsilon = 0.25$ (Fig. 2). Pressure fluctuations organize around the first acoustic mode, and three frequency stages occur for $M > 0.75$. These frequency stages

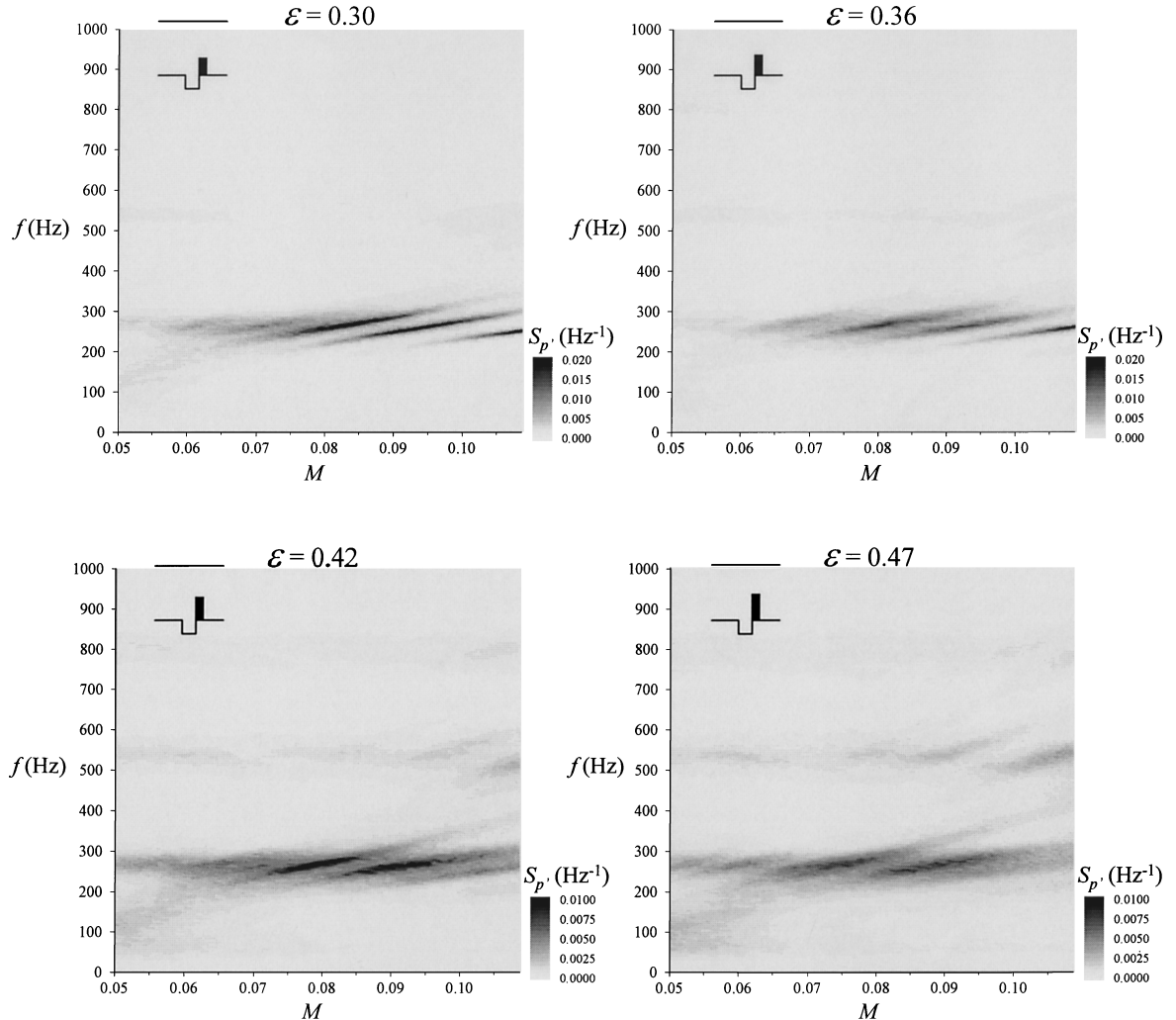


Fig. 10 Influence of the ε parameter on the pressure fluctuation spectra at the head end.

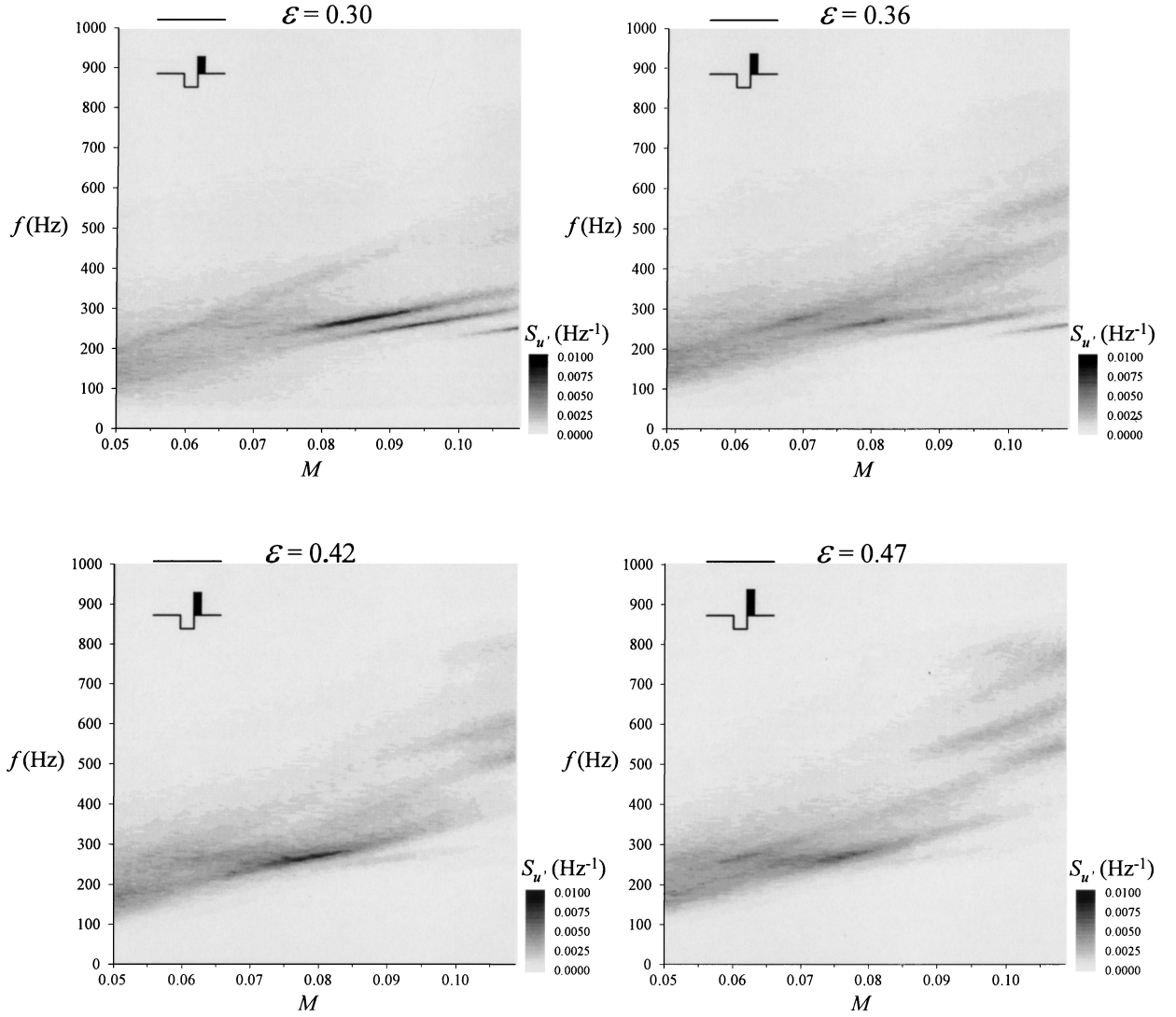


Fig. 11 Influence of the ε parameter on the velocity fluctuation spectra close to the obstacle location.

are still present for $\varepsilon = 0.36$, but the peak frequencies have become broadband. This trend is confirmed for $\varepsilon = 0.42$, where the fluctuating pressure energy is spread over a large band around the acoustic mode. Finally, by increasing the obstacle height to $\varepsilon = 0.47$, only two main frequency stages are observed for $M > 0.65$. Moreover, for large Mach numbers ($M > 0.1$), the excitation of frequencies close to the second acoustic mode is observed ($f_2 = 530$ Hz). Thus, when the area of passage is restricted in the obstacle section, the occurrence of narrow-band frequency peaks in the resonant sound pressure disappears. The background noise increases, whereas the periodic character of fluctuations is weakened in favor of a more random behavior.

Spectra of velocity fluctuations recorded in the $X = 0.15$ section for the earlier ε levels studied are shown in Fig. 11. As observed for $\varepsilon = 0.25$ (Fig. 2), pressure and velocity fluctuations have the same periodic components for the two first configurations ($\varepsilon = 0.3$ and $\varepsilon = 0.36$). Despite the appearance of broadband spectra when ε increases, frequency stages occurring in the velocity field are similar to those observed in the resonant field. However, for the last two configurations ($\varepsilon = 0.42$ and $\varepsilon = 0.47$), velocity fluctuations do not reproduce all of the pressure fluctuations. The evolution of pressure spectra with the Mach number shows two main frequency stages for these ε levels, whereas only the first stage is represented in velocity spectra (Fig. 11). At the same time, the excitation of higher frequencies is observed between $f = 500$ and 600 Hz for $\varepsilon = 0.42$ and between $f = 500$ and 800 Hz for $\varepsilon = 0.47$. The effect of increasing the height of the obstacle, therefore, implies different forms of

flowfield behavior. First, random fluctuations are favored; this most likely arises from an increase in the background turbulence velocity due to the perturbations induced by the obstacle. Second, the velocity frequency scales grow larger as ε increases. In fact, because the section at $X = 0$ decreases with ε , the velocity levels increase, and this implies higher frequencies according to linear stability theory.³¹ The fluctuating velocity field in the wake of the obstacle shows the involvement of natural instability frequencies and is not the same as the pressure field. Velocity spectra for $\varepsilon = 0.42$ are plotted again in Fig. 12 with spectra of velocity fluctuations recorded in the $X = 0.64$ section for two transverse probe locations. Close to the upper wall ($Y = 0.86$, Fig. 12b), spectral components differ compared with the one observed downstream from separation (Fig. 12a). The random behavior in velocity fluctuations is more pronounced, but the frequency stage is still observed. On the contrary, the excitation of frequencies between $f = 500$ and 600 Hz present at $X = 0.15$ is not observed at $X = 0.64$. Instead, a second frequency stage characterizes the velocity spectra for $M > 0.085$. Then, two frequency stages are observed at $X = 0.64$, similar to the pressure fluctuation behavior shown in Fig. 10. The frequencies corresponding to the second frequency stage at $X = 0.64$ are shown on the velocity map at $X = 0.15$ ($f_{\text{inst}}/2$); the evolution of twice the frequencies f_{inst} is also plotted. Note that at separation the shear layer oscillates at the frequency f_{inst} for $M > 0.9$, whereas far downstream from the obstacle location, the first subharmonic of f_{inst} is dominant. A merging process is, therefore, responsible for the second frequency stage observed in velocity spectra, as well as pressure spectra. Ho and Huang³²

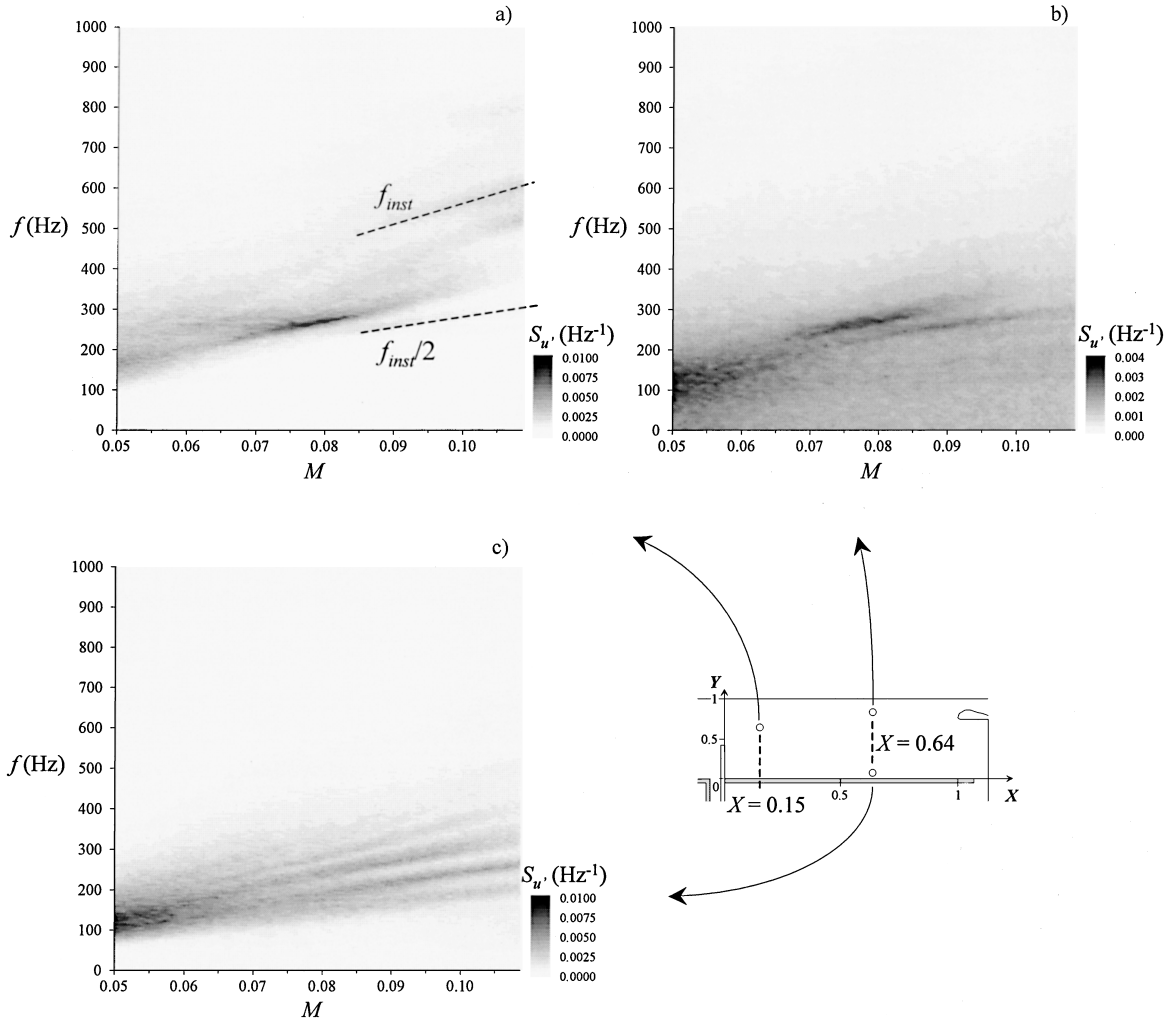


Fig. 12 Investigation of the fluctuating flowfield for $\varepsilon = 0.42$: velocity spectra a) close to the obstacle location, b) in the rear end of the chamber, and c) in the vicinity of the injecting wall.

also observed the merging of two vortices for mixing layers when the forcing frequency was one-half of the natural frequency of the layer. The spectra of velocity fluctuations recorded at $X = 0.64$ in the vicinity of the injecting wall ($Y = 0.05$) is shown in Fig. 12c. The two frequency stages are detectable, even if the frequency peaks are much less pronounced compared with the results obtained for $\varepsilon = 0.25$ (cf. Fig. 2c). Even for high-Mach-number levels, where the coupling phenomenon occurs, spectra are broadband. The same data analysis was conducted for the $\varepsilon = 0.47$ configuration and likewise showed the merging process occurring in the shear layer. However, close to the injecting wall, the frequency stages were not observed; strong random behavior does not allow extraction of dominant characteristic frequencies.

Thus, the influence of the height of the obstacle on the flowfield behavior can be described as follows. As shown in Fig. 13 for the $\varepsilon = 0.3$ configuration and as was observed for $\varepsilon = 0.25$, the streamlines bypass the obstacle and hit the wall where vorticity generation occurs; the shear layer vortices result in wall structures that develop along the injecting wall. When H_{obs} is increased, the reattachment length increases. Therefore, the appearance of the wall vortices is delayed downstream, as is the case for $\varepsilon = 0.36$. For high ε levels, the vorticity generation mechanism at wall should disappear. However, at the same time, velocity levels become higher at flow separation, which increases the frequencies involved. The low-frequency forcing at the first acoustic mode forms a wavy shear layer that causes a pairing phenomenon, and two vortices pair before reattachment. This induces a drop in passage frequency associated with relatively large shear layer growth. Acharya et al.³³ examined the effect of subharmonic forcing on a curved, reattaching shear layer behind a

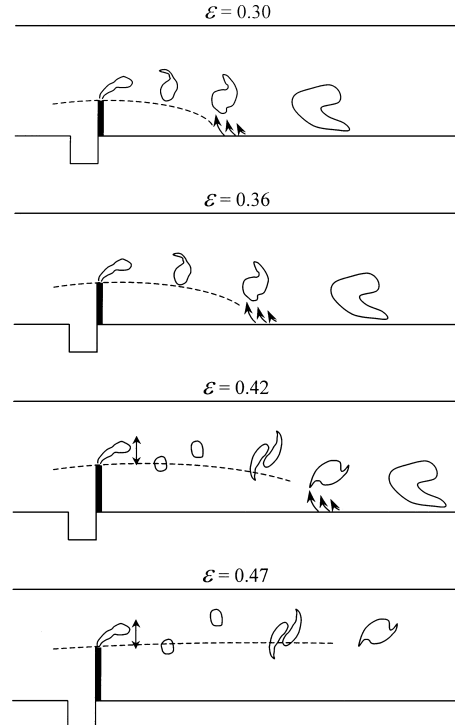


Fig. 13 Flow pattern schematic for different values of ε .

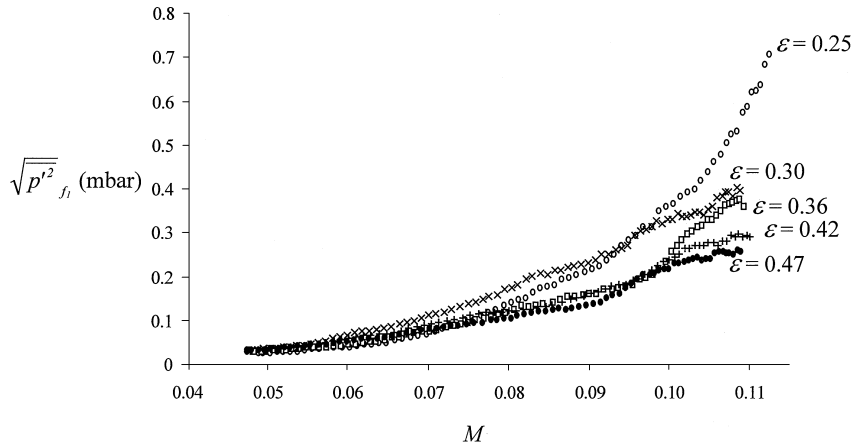


Fig. 14 Influence of the ε parameter on the pressure fluctuation level associated with the first acoustic mode.

rib in a ribbed-duct flow. In their experiments, the pairing is accompanied by significant entrainment and shear-layer growth, which leads to a reduction in the reattachment length. Here, even for high ε values, the induced field produced by the resulting large eddy is strong enough to interact with the injected flow; the wall vortices are still observed, but their appearance is delayed in the rear end of the chamber, as seen for $\varepsilon = 0.42$. Even if the spectral content of the pressure gradient is more broadband, vorticity generation occurs but the generated velocity field is not highly structured. Finally, for the highest ε values studied ($\varepsilon = 0.47$, for example), the shear layer vortices are convected in the flow in the direction of the upper wall, and the shear layer no longer reattaches. The frequency stages are caused by a pairing phenomenon, but the convection of the resulting large structure remains without effect on the wall where no vorticity generation occurs. Therefore, the vortices separating at the top of the obstacle are not fed by wall injection.

A direct consequence of such an effect is shown in Fig. 14. The evolution of the rms of the pressure fluctuations associated with the f_1 mode is plotted vs the Mach number for all of the configurations tested. These levels were computed from pressure spectra by integrating the power spectral density over the range $200 < f < 330$ Hz, that is, 30 Hz lower and higher than the lowest and the highest frequencies involved, respectively. For the reference configuration ($\varepsilon = 0.25$), the energy increases regularly over the entire Mach number range. For $\varepsilon = 0.3$, this evolution remains similar. The levels are, nonetheless, higher for $M < 0.095$ and lower for $M > 0.095$ to reach approximately half the levels obtained for $\varepsilon = 0.25$ at the highest Mach numbers. For the other ε values, the changes are similar up until $M = 0.1$. For higher M values, an amplification is observed and is weaker insofar as ε is small. Therefore, when the height of the obstacle is increased, the vorticity generation at wall disappears, and this attenuates the noise level.

IV. Conclusions

Experiments are presented to study the influence of an obstacle on the flowfield generated in a channel with porous walls through which air at ambient temperature is injected. A nozzle at the rear end represents a potential impingement area for vortices. For small Mach numbers, the unforced flow does not reattach downstream from the obstacle. At a sufficient noise level, an acoustic forcing close to the natural instability of the flow regularizes the vortex formation. The similar velocity behavior observed downstream from the obstacle location and in the vicinity of the injecting wall spotlights a significant increase in the entrainment of the shear layer. A reattaching, curved shear layer develops downstream from the obstacle. The interaction with the injected flow leads to a vorticity generation through the axial pressure gradient. A wall vortex development is observed downstream, and the flowfield behaves like a well-known wall injection flow. A feedback loop pilots the instability development, and the frequency stages observed result from a modification

with the Mach number of the number of vortices between separation and impingement to conserve an oscillation frequency close to the first acoustic mode of the chamber.

By the increase in the height of the obstacle, the velocity fluctuation frequencies are increased. The first acoustic mode resonance induces a forcing at the first subharmonic of the shear layer, leading to the pairing of two vortices before reattachment. Finally, for relatively high obstacle height, despite the vortex merging process, the flow does not reattach, and no vorticity generation occurs. This results in a decrease in noise generation and resonance quality.

An interesting topic would consist in modifying the axial pressure gradient at wall to influence the vorticity generation. This could be observed, for example, in a channel where the section gradually increases or decreases with the axial location to moderate or amplify the increase of the velocity due to sidewall injection. On the other hand, this point would imply a gradual modification of the injection Reynolds number, whose effect is to delay downstream or upstream the appearance of turbulence.

This work could represent a starting point for cooling flows by wall transpiration. The mixing of a cold gas injected through porous walls in a hot main flow could be more efficient by forcing the creation of wall structures that would enhance heat transfers.

Acknowledgments

This work has been supported by the Centre National d'Etudes Spatiales for the study of the instabilities of the MPS/P230 of Ariane 5. The authors give special thanks to Michel Pons, Director of the Solid Propulsion Department, for his tireless aid. The authors are particularly grateful to Mauro Augelli for his continuing support of this project.

References

- ¹Traineau, J. C., Hervat, P., and Kuentzmann, P., "Cold-Flow Simulation of a Two-Dimensional Nozzleless Solid Rocket Motor," AIAA Paper 86-1447, June 1986.
- ²Beddini, A. R., "Analysis of Injection Induced Flows in Porous Walled Duct with Application to Aerochemistry of Solid Propellant Motor," Ph.D. Dissertation, Mechanical and Aerospace Engineering, Rutgers Univ., New Brunswick, NJ, Oct. 1981.
- ³Taylor, G. I., "Fluid Flow in Regions Bounded by Porous Surface," *Proceedings of the Royal Society of London, Series A: Mathematical and Physical Sciences*, Vol. 234, No. 1199, 1956, pp. 456–475.
- ⁴Culick, F. E. C., "Rotational Axisymmetric Mean Flow and Dumping of Acoustic Waves in Solid Propellant Rocket Motor," *AIAA Journal*, Vol. 4, No. 8, 1966, pp. 1462–1464.
- ⁵Yeh, Y. P., Heaman, J. P., Ramachandran, N., and Smith, A. W., "Subscale Cold Flow Simulation of the Port Flow in Solid Rocket Motors," AIAA Paper 94-3294, June 1994.
- ⁶Yagodkin, V. I., "Use of Channels with Porous Walls for Studying Flows Which Occur During Combustion of Solid Propellants," *Proceedings of the 18th Aeronautics Congress, FTD-ID(RS)T*, Vol. 3, 1967, pp. 69–79 (translation).

⁷Varapaev, V. N., and Yagodkin, V. I., "Flow Stability in a Channel with Porous Wall," *Izvestiya Mekhanika Zhidkosti i Gaza*, Vol. 4, No. 5, 1976, pp. 91–95 (translated in *Fluid Dynamics*, Vol. 4, No. 5, 1976, pp. 91–95).

⁸Eckert, E. R. G., and Rodi, W., "Reverse Transition Turbulent–Laminar for Flow Through a Tube with Fluid Injection," *Journal of Applied Mechanics*, No. 87, 1968, pp. 817–819.

⁹Pennell, W. T., Eckert, E. R. G., and Sparrow, E. M., "Laminarization of Turbulent Pipe Flow by Fluid Injection," *Journal of Fluid Mechanics*, Vol. 52, No. 3, 1972, pp. 451–464.

¹⁰Dunlap, R., Blackner, A. M., Waugh, R. C., Brown, R. S., and Willoughby, P. G., "Internal Flowfield Studies in a Simulated Cylindrical Port Rocket Chamber," *Journal of Propulsion and Power*, Vol. 6, No. 6, 1990, pp. 690–704.

¹¹Lupoglazoff, N., and Vuillot, F., "Numerical Simulations of Parietal Vortex-Shedding Phenomenon in a Cold Flow Set-Up," AIAA Paper 98-3220, July 1998.

¹²Casalis, G., Avalon, G., and Pineau, J. P., "Spatial Instability of Planar Channel Flow with Fluid Injection through Porous Walls," *Physics of Fluids*, Vol. 10, No. 10, 1998, pp. 2558–2568.

¹³Griffond, J., Casalis, G., and Pineau, J. P., "Spatial Instability of Flow in a Semi Infinite Cylinder with Fluid Injection Through Its Porous Walls," *European Journal of Mechanics. B, Fluids*, Vol. 19, No. 1, 2000, pp. 69–87.

¹⁴Avalon, G., Casalis, G., and Griffond, J., "Flow Instabilities and Acoustic Resonance of Channels with Wall Injection," AIAA Paper 98-3218, July 1998.

¹⁵Majdalani, J., and Van Moorhem, W. K., "Multiple-Scales Solution to the Acoustic Boundary Layer in Solid Rocket Motors," *Journal of Propulsion and Power*, Vol. 13, No. 2, 1997, pp. 186–193.

¹⁶Kirkkopru, K., Kassoy, D. R., and Zhao, Q., "Unsteady Vorticity Generation and Evolution in a Model of a Solid Rocket Motor," *Journal of Propulsion and Power*, Vol. 12, No. 4, 1996, pp. 646–654.

¹⁷Zhao, Q., Staab, P. L., Kassoy, D. R., and Kirkkopru, K., "Acoustically Generated Vorticity in an Internal Flow," *Journal of Fluid Mechanics*, Vol. 413, 2000, pp. 247–285.

¹⁸Staab, P. L., Zhao, Q., Kassoy, D. R., and Kirkkopru, K., "Co-Existing Acoustic-Rotational Flow in a Cylinder with Axisymmetric Sidewall Mass Addition," *Physics of Fluids*, Vol. 11, No. 10, 1999, pp. 2935–2951.

¹⁹Shu, P. H., Sforzini, R. H., and Foster, W. A., "Vortex-Shedding from Solid Rocket Propellant Inhibitors," AIAA Paper 86-1418, June 1986.

²⁰Vetel, J., Plourde, F., and Doan-Kim, S., "Mixing Effects Between Self-Sustained Oscillations and Unstable Hydrodynamic Behavior near Injecting Walls," *AIAA Journal*, Vol. 39, No. 8, 2001, pp. 1455–1468.

²¹Vetel, J., Plourde, F., and Doan-Kim, S., "Dynamics of an Internal Flow-field Driven by Two Hydrodynamic Instabilities," *AIAA Journal*, Vol. 41, No. 3, 2003, pp. 424–435.

²²Bendat, J. S., and Piersol, A. G., *Random Data Analysis and Measurement Procedures*, Wiley-Interscience, New York, 1986, Chap. 3.

²³Blevins, R. D., "The Effect of Sound on Vortex Shedding from Cylinders," *Journal of Fluid Mechanics*, Vol. 161, 1985, pp. 217–237.

²⁴Avalon, G., Ugurtas, B., Grisch, F., and Bresson, A., "Numerical Computations and Visualization Tests of the Flow Inside a Cold Gas Simulation with Characterization of a Parietal Vortex Shedding," AIAA Paper 2000-3387, July 2000.

²⁵Venugopal, P., Najjar, F. M., and Moser, R. D., "DNS and LES Computations of Model Solid Rocket Motors," AIAA Paper 2000-3571, July 2000.

²⁶Eaton, J. K., and Johnson, J. P., "A Review of Research on Subsonic Turbulent Flow Reattachment," *AIAA Journal*, Vol. 19, 1981, pp. 1093–1100.

²⁷Yamada, K., Goto, M., and Ishikawa, N., "Simulative Study on the Erosive Burning of Solid Rocket Motors," *AIAA Journal*, Vol. 14, No. 9, 1976, pp. 1170–1176.

²⁸Vetel, J., Plourde, F., and Doan Kim, S., "Influence of Hydrodynamic Conditions on the Vortex Shedding Phenomenon," AIAA Paper 2000-2000, June 2000.

²⁹Rossiter, J. E., "Wind-Tunnel Experiments on the Flow over Rectangular Cavities at Subsonic and Transonic Speeds" Aeronautical Research Council, Ministry of Aviation, Reports and Memoranda 3438, London, Oct. 1964.


³⁰Ho, C. M., and Nosseir, N. S., "Dynamics of an Impinging Jet. Part 1: The Feedback Phenomenon," *Journal of Fluid Mechanics*, Vol. 105, 1981, pp. 119–142.

³¹Freymuth, P., "On Transition in a Separated Laminar Boundary Layer," *Journal of Fluid Mechanics*, Vol. 25, No. 4, 1966, pp. 683–704.

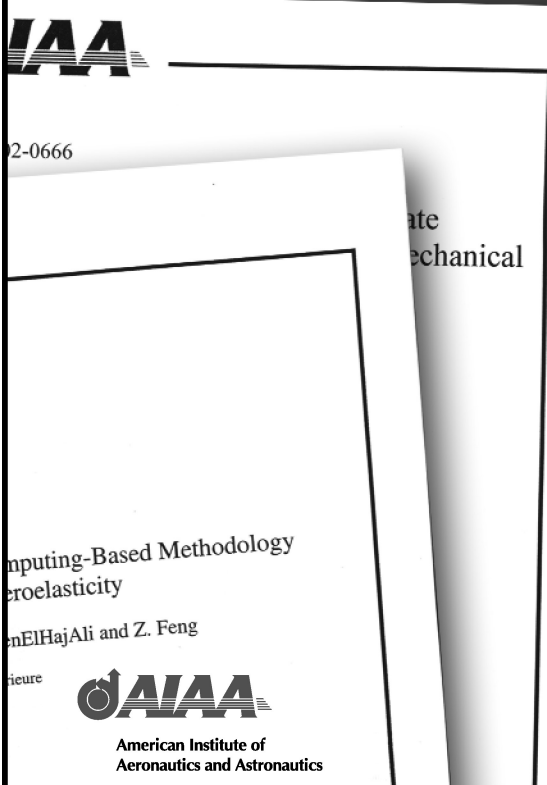
³²Ho, C. M., and Huang, L. S., "Subharmonics and Vortex Merging in Mixing Layers," *Journal of Fluid Mechanics*, Vol. 119, 1982, pp. 443–473.

³³Acharya, S., Myrum, T. A., and Inamdar, S., "Subharmonic Excitation of the Shear-Layer Between Two Ribs: Vortex Interaction and Pressure Field," *AIAA Journal*, Vol. 29, No. 9, 1991, pp. 1390–1399.

A. Plotkin
Associate Editor


Register Purchase

AIAA MEETING PAPERS ONLINE!




2-0666

ate
mechanical

Computing-Based Methodology
eroelasticity

enElHajAli and Z. Feng

ieure



American Institute of
Aeronautics and Astronautics

Exhibit

Each year, AIAA publishes more than 4000 technical papers presented at AIAA conferences. These papers contain the most recent discoveries in aerospace and related fields. No other organization offers this depth and breadth in the aerospace field.

You now have immediate access to more than 20,000 technical papers online!

Beginning with 1996 and adding about 4,000 papers every year, AIAA's online archive allows you to search for the latest developments in:

Aerodynamics • Aerodynamics • Guidance • Structures • Fluids • Propulsion • Controls • Modeling and Simulation • Flight Mechanics • and more...

Search and purchase only those papers that fit your needs. Papers are delivered in pdf format. Search by:

Title • Keyword • Author • AIAA Paper Number • Conference Title • Publication Year

Click on "Citations Database" from the AIAA Web site at

www.aiaa.org